The Rise of Buoyant Magnetic Structures through Convection with a Background Magnetic Field

Christina Pontin,[1] Bhishek Manek [ID],[2] and Nicholas Brummell [ID][2]

[1]*Department of Applied Mathematics,*
School of Mathematics, University of Leeds,
Leeds, LS2 9JT, UK
[2]*Department of Applied Mathematics, Jack Baskin School of Engineering, University of California Santa Cruz,*
1156 High Street, Santa Cruz, California 95064, USA

ABSTRACT

Motivated by observations at the solar surface of sunspots embedded in active regions, it is widely believed that large scale, strong magnetic flux emerges from the Sun's deep interior in the form of arched, cylindrical tube-like structures, often known simply as flux tubes. Here, we continue a line of research that examines the different dynamics encountered when one considers these structures as concentrations in a volume-filling magnetic field rather than as isolated magnetic structures in a field-free background. In particular, here, via numerical simulations, we consider the buoyant rise of magnetic flux concentrations from their formation in a deep radiative zone, through a turbulent overshooting convection zone that self-consistently arranges a volume-filling large-scale background field. This work is complementary to earlier papers that considered such dynamics in the absence of convection, where the form of the background field had to be assumed. That earlier work established the existence of a selection mechanism that created an increased likelihood of successful rise for magnetic structures that had one sense of twist (measured relative to the orientation of the background field), and a decreased likelihood for the other sense. This mechanism, when applied to the solar context, is commensurate with the solar hemispherical helicity rule (SHHR) and therefore may be considered as a possible contributor to this rule. This paper establishes the robustness of this selection mechanism in a more realistic model incorporating convection and therefore a self-consistent background field. The overshooting convection transports (or "pumps") any initial large-scale horizontal magnetic field out of the convective region, accumulating it in a layer at the edge of the overshooting region. Flux tubes placed within this layer (as if they were forming there) then experience the selection mechanism where some rise and some do not, depending on their twist characteristics (relative to the background field). Convection only weakly influences the selection mechanism, since the mechanism is enacted at the initiation of the rise, at the edge of the overshoot zone. Convection does however add another layer of statistical fluctuations to the bias, which we investigate by Monte Carlo-like suites of simulations in order to explain variations in the SHHR.

1. INTRODUCTION

Observations of active regions and their sunspots have arguably had the largest influence on our understanding of the operation of the global dynamo that powers the magnetic activity of the Sun. That these objects, first associated with the magnetic field by Hale (1908), emerge from the highly turbulent plasma and yet obey a set of strict rules, is quite remarkable. Sunspots occur in pairs, with a leading polarity and a trailing polarity that switches cyclically with a period of about 11 years (Hale's Polarity Laws), and with a definite tilt of the leading object towards the equator (Joy's Law; Hale et al. (1919)). So-called "butterfly diagrams" of tracers

of this cyclic activity exhibiting the regular regeneration of magnetic field strongly suggest that a dynamo is likely responsible for this behaviour.

The prevailing theory behind these observations attributes active regions and sunspots to the emergence of elements of strong toroidal magnetic field through the visible surface of the Sun (Parker 1975). If cylindrical or tube-like structures of toroidal flux were to arch up through the visible solar surface, then the opposite polarity of the sunspot pairs would be explained by the oppositely-directed field in the legs of these arches where they pierce the solar surface. Furthermore, it is plausible that some interaction of this emerging flux loop with the background solar rotation could lead to a writhe of

the structure that accounts for the Joy's Law tilt. The cyclic change in polarity would have to be imposed during the origin of the field, requiring a reversal of the toroidal field.

It has long been thought that strong toroidal field is likely generated deep in the solar interior, towards the base of the convection zone or in the tachocline, where strong shear in the form of differential rotation can amplify fields significantly. Since these processes are far removed from the surface, magnetic buoyancy is invoked as a transport mechanism between the two regions (Parker 1975). The concept of magnetic buoyancy can loosely be described as the situation where a strong concentration of magnetic field contributes significant magnetic pressure to the total pressure. Under the simple assumptions that the total pressure and the temperature equilibrate quickly, this leads to a decrease in the density associated with the magnetic concentration that results in an upwards buoyant force. This process can be cast more formally as an instability (Acheson 1979), and a great success of simulations of magnetic buoyancy instabilities has been that they naturally exhibit the creation of rising, arching, tube-like structures of magnetic field, akin to what was envisaged for the solar case (e.g. Matthews et al. 1995; Vasil & Brummell 2008).

Some of the more recent observations of magnetically-active areas of the sun have focused on a relatively new signature of the activity, namely, the magnetic helicity of these regions (see e.g. Pevtsov et al. 2014, for a complete review). Magnetic helicity is defined as $H_m = \int_V \mathbf{A} \cdot (\nabla \times \mathbf{A}) \, \mathrm{d}V$. Here, $\mathbf{B}$ is the magnetic field, and $\mathbf{B} = \nabla \times \mathbf{A}$, so that $\mathbf{A}$ is a vector potential defining the divergenceless magnetic field. Since $\mathbf{A}$ is not uniquely defined, nor can it be directly measured in observations, a more commonly-used measure is current helicity, $H_c = \int_V \mathbf{B} \cdot (\nabla \times \mathbf{B}) \, \mathrm{d}V$. The current helicity is a measure of the twist, writhe and connectedness of the magnetic field (see e.g. Moffatt 1969). These quantities are important for two main reasons. Firstly, H_m is an invariant of the ideal MHD equations and thereby provides strong constraints on those dynamics. Secondly, the release of energy from twisted magnetic field is commonly cited as one of the major sources powering eruptive events in the solar atmosphere (e.g. Low 1996; Amari et al. 2003; Nindos & Andrews 2004). The origin of such twist is therefore important. Since H_c is more measurable, it is often used as a proxy for H_m, although it is unclear under what circumstances this is useful (Seehafer 1990; Pevtsov et al. 1995; Abramenko et al. 1997; Bao & Zhang 1998).

The most striking result from observations of the current helicity in active regions is that, once again, such dynamics seem to be remarkably ordered, considering the turbulent environment through which the magnetic structures emerge. It has been found that the sign of the current helicity, when averaged over active region areas, has a strong dependence on which solar hemisphere it belongs to: in the Northern hemisphere, in general the helicity is negative, whereas in the Southern hemisphere, it is positive (see e.g. Pevtsov et al. 2014) . This is a trend and not a strict rule, only being obeyed approximately 60-80% of the time. However, this trend is independent of which half of the 22-year solar cycle is examined; that is, it is independent of the polarity of the sunspots pairs, or the direction of the toroidal field making up the sunspot structures. This set of rules is known collectively as the Solar Hemispherical Helicity Rule (SHHR).

The origin of this rule is clearly of interest, and there have been a number of theories put forward. This paper presents the most complete and dynamically-realistic version to date of the dynamics postulated by one of these potential theories, previously developed in Manek et al. (2018) and Manek & Brummell (2021) (hereinafter known as Papers 1 and 2). There are indeed other reasonable theories apart from the one pursued here (see e.g. Longcope et al. 1996; Choudhuri et al. 2004), and it is entirely plausible, if not perhaps even likely, that the processes conceived in each of these theories all contribute to the overall helicity budget of a rising magnetic structure to some degree. The introduction of Paper 2 contains more details and the pros and cons of each theory, so they are not repeated again here. Instead, we follow the theory of Papers 1 and 2 and examine the robustness of these ideas under conditions that are more representative of solar conditions than were examined in those earlier works.

The theory proposed in Papers 1 and 2 arises from adopting a slightly different perspective from those used previously in the modelling of the rise of structures by magnetic buoyancy. In general, earlier work done in this context has proceeded mainly along three fronts. Firstly, there have been many studies of the rise of pre-conceived, *isolated*, tube-like magnetic structures. Here, the key point is that the structures are isolated in the sense that they are embedded in an environment that is free of other magnetic field. Such studies have been performed under the thin flux tube approximation (e.g. Spruit 1981) and, more realistically, where the tube has a finite cross-section (e.g. Moreno-Insertis 1983, 1986; Choudhuri 1989; D'Silva & Choudhuri 1993; Fan et al. 1993, 1994; Caligari et al. 1995; Longcope & Klapper

1997). An interesting discovery here was that locally-azimuthal field in the tube is required in order to create twisted field lines that supply a centrally-directed tension that provides coherence to the tube during its rise (Moreno-Insertis & Emonet 1996). Without sufficient twist, the tubes are ripped apart by the trailing vortices they generate in their wake. The second class of modelling efforts concerns true instabilities of layers of magnetic field (see e.g. Acheson 1979; Cattaneo & Hughes 1988; Matthews et al. 1995; Vasil & Brummell 2008). Here, magnetic structures are not initially present, but horizontal layers of magnetic field containing sufficiently strong vertical gradients are unstable to magnetic buoyancy instabilities and therefore evolve to produce such structures. Typically, tube-like structures with a mushroom-like cross-section are created, that can arch and kink in simulations if they are three-dimensional. The final category is that of global dynamo simulations. Some spherical shell simulations at certain parameters show the production of strong bands of toroidal field amid the convection, including rising segments that again look similar to the concept of emerging flux tubes.

It should be noted that both of the latter two categories can end up with the existence of concentrated strong magnetic structures embedded in a large-scale background field (usually the field from which the structures were created). This is contrary to many of the earlier studies in the first category. The work performed in Papers 1 and 2 was a simple attempt at examining the different dynamics of magnetic concentrations embedded in a volume-filling large-scale background field without specifically having to be concerned about the process that created the magnetic structures. To that end, Papers 1 and 2 examined the dynamics of a preconceived flux concentration (often still colloquially referred to as a "flux tube" for convenience) embedded in a chosen background field in an initially quiescent, adiabatically-stratified fluid layer. These numerical studies were performed in a Cartesian 2.5D domain, where all three components of vector fields are kept, but assumed to be independent of one horizontal direction (say, y), so that only a two-dimensional domain (in the other horizontal direction and the vertical, say x and z respectively) is actually computed. This allows magnetic structures to have twist in a two dimensional calculation. That is, the structures are typically initially confined to a circular region and contain both axial (y) and locally-azimuthal field (in x and z). Papers 1 and 2 then also imposed a horizontal (in x) magnetic field that had an assumed variation in the vertical (z) so that the flux tube was a structure embedded in this larger-scale field.

Papers 1 and 2 remarkably found that, for a certain region of parameter space (termed the Selective Rise Regime or SRR), there was a selection mechanism that dictated different dynamics for differently twisted initial tubes (relative to a fixed background field direction). It was found that tubes that had twist such that the locally azimuthal field at the bottom of the tube aligned with the background field had a tendency to be more likely to rise than tubes whose twist was such that the azimuthal field was aligned at the top. These selective dynamics only occur for intermediate relative strengths of the tube and the background field. If the tubes are relatively weak, both signs of twist cannot rise; if the tubes are relatively strong, both signs of tubes rise. If the background field strength is between $\sim 5-15\%$ of the tube strength (roughly, for the other parameters considered in Papers 1 and 2), then one sign twist is rises and the other does not. The reason for the existence of the selection effect is the differential influence of the background field on internal tension forces in the tube. Where the background field and the locally-azimuthal field of the tube align, the tension forces are increased, and they are reduced where the two components are anti-aligned. When the enhancement is at the bottom of the structure and the reduction is at the top, a net tension force acts upwards, in concert with the buoyancy forces, enhancing the opportunity for rise. When the alignment is the other way around, net tension forces in the tube act downwards and oppose buoyancy, reducing the likelihood of rise. Most remarkably, if translated into the solar context, the preferred signs of twist translate into the correct helicities to obey the SHHR. Paper 2 explored this selection mechanism and the SRR in great detail, and included an explanation of the dynamics via a simple mathematical model. An intriguing point is that the existence of the SRR suggests that violations to the rule are entirely plausible, if twist is assumed to be created initially with some distribution. Paper 2 confirmed this via synthetic SHHR maps generated from Monte Carlo simulations of multiple tubes with random twist strengths and locations. The biggest difference between this model and other theories is that all the other theories essentially require a rising tube to *acquire* the correct twist (by some method) as it rises. In the models of Papers 1 and 2, instead, all signs of twist are assumed to be created randomly (as seems to be the case in simulations magnetic buoyancy instabilities, see e.g. Matthews et al. (1995); Vasil & Brummell (2008)) and then the selection mechanism *acts as a filter*, allowing a certain sign of twist to rise preferentially (but with significant violations to the rule).

The simulations examined in Papers 1 and 2 employed highly simplified models of the background dynamics. The magnetic structures simply buoyantly rose in an initially quiescent, adiabatic fluid layer, and the large-scale background field was artificially imposed as an exponential function that decreased upwards. These choices were supposed to represent the thermodynamic background state that would result from a well-mixed convective state and also the large-scale magnetic field that would result from transport by convection in such a state, even though the actual convection was not included. This paper aims to relax these simplifications and study the fully convective problem. Prevailing theories for the origin of emerging active region flux have flux tubes formed most likely in the tachocline, and therefore rising structures must traverse perhaps the upper radiative zone, the overshoot zone and the convection zone in their rise towards emergence at the surface. Here, in this study, we model all of these zones, and examine rise through them. However, we note that we still make no attempt to model any process that creates the magnetic concentrations from the large-scale field since we exclude the shear of the tachocline.

We do, however, pay great attention to modelling the overshooting convection that should be present at the base of the solar convection zone, and the magnetic fields that might be associated with it. Overshooting convection has been much studied in the astrophysical context (see e.g. Hurlburt et al. 1989; Zahn 1991; Hurlburt et al. 1994; Singh et al. 1995; Brummell et al. 2002; Korre et al. 2019). When a convectively-unstable layer is abutted by a convectively-stable layer, the motions of the convection are not confined to the convective layer alone, and can "overshoot" into the adjacent stable layer, where they are buoyantly decelerated. If the overshooting motions are sufficiently strong enough to mix the thermodynamic background close to adiabatic in the overshoot zone, the effect is termed "penetration" rather than overshoot. There is much astrophysical interest in the degree of overshoot and penetration since such motions imply extra mixing, and much attention has been applied to the extent of such motions and mixing since it may have a significant impact on stellar evolution.

A particularly intriguing magnetic effect also occurs in overshooting convection. Magnetic field that exists on much larger scales than the convective turbulence can be expelled from the convective region to form a layer at the edge of the overshoot zone, in a process known generically as "magnetic pumping" (see e.g. Dorch et al. 2001; Tobias et al. 1998, 2001a; Korre et al. 2021). There are a number of effects that can contribute to such expulsion but likely the dominant one is the transport of large-scale field down a gradient of turbulent intensity. This process has been characterized in mean-field models by the γ-effect (Rädler 1968). Clearly such a gradient exists between the convection zone and the radiative layer below the overshoot. The comprehensive three-dimensional simulations of Tobias et al. (2001a) showed that mean field would accumulate at the lower edge of the overshoot zone even though there was a constant circulation of smaller-scale magnetic field leaving and arriving at the layer by magnetic buoyancy and advection effects. Such a layer was only slowly eroded by diffusion and boundary effects.

This paper therefore extends the work of Papers 1 and 2 substantially in two main ways. Firstly, the magnetic concentration evolves by magnetic buoyancy through two vertically-stacked regions. The flux concentration begins in a deeper layer that is initially convectively-stable (representing a radiative zone, or a tachocline), and then, if it buoyantly rises, it transits through a convection zone. This is in contrast to the previous work where the buoyant rise only transited through a single quiescent adiabatic layer. Secondly, the presence of this two-layer system of overshooting convection serves to generate a self-consistent distribution of any imposed large-scale background field by magnetic pumping. In the previous works of Papers 1 and 2, the profile of the background field was merely imposed artificially.

The structure of this paper is as follows: in § 2, we outline our two-layer magnetoconvection model, including the governing equations and the numerical methods used; in § 3.1, we exhibit results from simulations only incorporating overshooting convection in 2.5D in a similar manner to the 3D results of Tobias et al. (2001b); in § 3.2, we study under what conditions an *isolated* rising flux concentration is able to transit the overshooting convection, as a pre-cursor to examining the effect of the existence of a background field; in § 3.3, without any flux tubes present, we examine the self-consistent rearrangement of a large-scale (mean) horizontal magnetic field by magnetic pumping in 2.5D in a similar manner to the 3D simulations of Tobias et al. (2001b); in § 3.4, for a canonical set of parameters, we combine the acquired knowledge into simulations that study the rise of a flux concentration in a two-layer overshooting convective system incorporating a self-consistent large-scale (mean) background magnetic field ; in § 4 and the full paper we examine the influence of various parameters of the model and check the statistical robustness of the results. Ultimately, we draw conclusions in particular, noting that the selection mechanism found in Papers 1 and 2 still operates in this far more complex situation.

2. MODEL AND METHODS

This study extends the work of Papers 1 and 2. As in those earlier works, this paper considers the evolution of a flux concentration in a large-scale background field. However, this paper is substantially different in two main ways. Firstly, the concentration (often referred to as a "flux tube" merely for convenience) evolves by buoyancy through two vertically-stacked regions. The flux concentration begins in a deeper layer that is initially convectively-stable (representing a radiative zone, or a tachocline), and then, as it buoyantly rises, it transits through a convection zone. This is in contrast to the previous work where the buoyant rise only transited through a single quiescent adiabatic layer. Secondly, the presence of this two-layer system of overshooting convection serves to generate a self-consistent distribution of the large-scale background field by magnetic pumping. In the previous works of Papers 1 and 2, the profile of the background field was merely imposed artificially.

We use the formulation used in Tobias et al. (2001b) to establish two layer overshooting convection with a large-scale background field. In our initial study of the problem here, we consider a 2-D Cartesian domain (x, z), that contains a fully compressible ideal gas confined between two horizontal, impenetrable, stress-free boundaries. We keep all three components of the velocity and magnetic vector fields, but all components are independent of the missing third direction (i.e. $\partial/\partial y = 0$). This type of setup is often referred to as 2.5D. The Cartesian box is $x_{\mathrm{m}}d$ wide and $z_{\mathrm{m}}d$ deep, where d is the depth of the convection zone in the two layer system. We nondimensionalize our system using d, T_0 (the temperature at the upper boundary), ρ_0 (the density at the upper boundary) and B_0 (some measure of the initial field strength) as our units of length, temperature, density and magnetic field strength. The thermal sound crossing time at the top of the domain, $(d^2/((c_p - c_v)T_0))^{1/2}$, is our unit of time, where c_p and c_v are the specific heats of the fluid at constant pressure and constant volume respectively (and their ratio $\gamma = c_p/c_v$ will be used later). With these units, the governing non-dimensional equations (the conservation of mass, momentum and energy, the equation of state for a perfect gas, the induction equation and the divergence-free condition for magnetic fields) are (Tobias et al. 2001b)

$$\partial_t \rho + \nabla \cdot (\rho \mathbf{U}) = 0, \tag{1}$$

$$\partial_t (\rho \mathbf{U}) + \nabla \cdot (\rho \mathbf{U}\mathbf{U} - \alpha \mathbf{B}\mathbf{B}) =$$
$$-\nabla p_t + \sigma C_k \left[\nabla^2 \mathbf{U} + \frac{1}{3}\nabla(\nabla \cdot \mathbf{U}) \right] + \rho g \hat{z}, \tag{2}$$

$$\partial_t T + \nabla \cdot (\mathbf{U}T) + (\gamma - 2)T\nabla \cdot \mathbf{U} =$$
$$\frac{\gamma C_k}{\rho}\nabla \cdot (\kappa_z \nabla T) + \frac{\zeta C_k \alpha(\gamma - 1)}{\rho}|\nabla \times \mathbf{B}|^2 + V_\mu, \tag{3}$$

$$\partial_t \mathbf{B} = \nabla \times (\mathbf{U} \times \mathbf{B}) + C_k \zeta \nabla^2 \mathbf{B}, \tag{4}$$

$$\nabla \cdot \mathbf{B} = 0, \tag{5}$$

$$p_t = p_g + p_m = \rho T + \alpha \frac{|\mathbf{B}|^2}{2}. \tag{6}$$

Here, in nondimensional form, $\mathbf{U} = (u, v, w)$ is the velocity, $\mathbf{B} = (B_x, B_y, B_z)$ is the magnetic field, T is the temperature and ρ is the density. Note again that all quantities are only functions of (x, z) (where z varies downwards from the top). The total pressure, p_t, is the sum of the gas pressure, p_g ($= \rho T$ for an ideal gas), and the magnetic pressure, $p_m = \alpha|\mathbf{B}|^2/2$, where $\alpha = \sigma\zeta QC_k^2$ (where the latter parameters will be explained shortly). The rate of viscous heating is $V_\mu = (\gamma - 1)C_k\ \rho\sigma\partial_i u_j(\partial_i u_j + \partial_j u_i - (2/3)\nabla \cdot \mathbf{U}\delta_{ij})$.

Our two layer system consists of a convective layer (layer 1) overlying a convectively-stable layer (layer 2). This layering is enforced by a piecewise constant thermal conductivity (with a narrow smoothed junction between the two layers) that defines the two layers as being piecewise continuous polytropes when in a hydrostatic state. Since the total hydrostatic heat flux through the domain must remain the same at any depth, the thermal conductivities, κ_i, in the two layers can be described by the parameter $S = (m_2 - m_{\mathrm{ad}})/(m_{\mathrm{ad}} - m_1)$, related to the polytropic indices in the two layers, m_i, and the adiabatic index $m_{\mathrm{ad}} = 1/(\gamma - 1)$ ($= 1.5$ for an ideal monatomic gas where $\gamma = 5/3$):

$$\frac{\kappa_2}{\kappa_1} = \frac{m_2 + 1}{m_1 + 1} = \frac{S(m_{\mathrm{ad}} - m_1) + m_{\mathrm{ad}} + 1}{m_1 + 1}. \tag{7}$$

We choose $m_1 = 1$ always, and specify the temperature gradient in the hydrostatic upper layer as θ. The relative stability of the two domains is then measured by S, often referred to as the stiffness parameter (Hurlburt et al. (1994); Brummell et al. (2002)). Increasing S increases the relative stability ("stiffness") of the lower layer. Figure 1 shows the polytropic temperature and density profiles versus depth in the two layers for the three values of S that we use in these simulations, $S = 3, 7$ and 15.

The other dimensionless parameters that govern the system are as follows. The Rayleigh number,

$$Ra(z) =$$
$$\frac{\theta^2(m_i+1)}{\sigma C_{k_z}^2}\left(1 - \frac{(m_i+1)(\gamma-1)}{\gamma}\right)(1+\theta z)^{2m_i-1}, \quad (8)$$

is a derived measure that evaluates the competition between buoyancy driving (given in terms of the stratification inputs θ and m_i) and diffusive effects. This is therefore a measure of the the supercriticality and vigor of the convection. The Ra involves the non-dimensional thermal conductivity $C_{k_z} = C_k \kappa_z$, where $\kappa_z = \kappa_i/\kappa_1$ and $C_k = \kappa_1/\{d\rho_0 c_p[(c_p - c_v)T_0]^{1/2}\}$. which is different in the two layers. The Ra is a function of depth, and, in this study, the quoted value of Ra is evaluated at the middle ($z = 0.5$) of the unstable upper layer under the conditions of the initial polytrope.

The Prandtl number at a given depth is

$$\sigma_z = \frac{\mu c_p}{\kappa_z}, \quad (9)$$

where μ is the (constant) dynamic viscosity. The Prandtl number is depth-dependent, but $C_{k_z}\sigma_z = C_k\sigma$ is independent of κ_z and therefore is independent of depth. Any quoted Prandtl number is σ (the value in the upper layer). Similarly, the non-dimensional magnetic resistivity is controlled by a depth-dependent Schmidt number

$$\zeta_z = \frac{\eta c_p}{\kappa_z}, \quad (10)$$

but $C_{k_z}\zeta_z = C_k\zeta$ is independent of depth, and any quoted value is ζ.

The Chandrasekhar number,

$$Q = \frac{B_0^2 d^2}{\mu_0 \mu \eta}, \quad (11)$$

where μ_0 is the magnetic permeability, is a measure of the strength of the imposed magnetic field B_0 compared to diffusive effects. Note that the parameter truly governing magnetic effects is $\alpha = \sigma\zeta Q C_k^2$. This parameter determines the dynamic ratio of the gas pressure to the magnetic pressure, and is often referred to as the plasma β. Increasing Q (for fixed diffusivities) increases the dynamical back-reaction of any magnetic field on the flow field.

At the upper and lower boundaries of our domain, we apply impenetrable and stress-free boundary conditions

$$w = \partial_z u = \partial_z v = 0 \text{ at } z = 0, z_m, \quad (12)$$

which ensure that the mass flux and mechanical energy flux vanish on the boundaries conserving the total mass.

The boundary conditions on temperature are

$$T = 1 \text{ at } z = 0, \ \partial_z T = \frac{\kappa_2}{\kappa_1}\theta \text{ at } z = z_m, \quad (13)$$

therefore the imposed heat flux is the only flux of energy into and out of the system. The magnetic boundary conditions are specified as

$$B_x = B_y = 0 \text{ at } z = 0, z_m. \quad (14)$$

Note, that it is sufficient to impose boundary conditions only on the horizontal components of the magnetic field due to the solenoidality of **B**. We note that non-zero vertical gradients of the horizontal field can be present at the boundaries so that the magnetic energy can decrease with time, i.e. these can be "run-down" systems.

The domain is periodic in the horizontal in all variables.

This system is solved numerically using the same code and same pseudo-spectral methods as in Tobias et al. (2001a). The resolution typically used is 512×600 for the 6×2.5 aspect ratio 2D domain.

3. RESULTS

In order to achieve our goal of examining the effect of a self-consistent large-scale background field on the rise of a magnetic concentration through a convection zone, we must first complete some preparatory steps. First of all, we need to establish overshooting convection in our two layer system representing the base of the convection zone. Secondly, we must examine what strength of a flux tube is required for it to have enough buoyancy to rise through this convection. Thirdly, we must establish a vertical profile of pumped large-scale (mean) horizontal field with this overshooting convection (without the flux tube) to act as our self-consistent background field. Finally, we can then evolve the flux tube as a concentration amongst the volume-filling pumped background field in the convective simulation and examine the effect of that background field on the different signs of twist in the tube/concentration. We now describe each of these steps in detail.

3.1. Convection in 2D

We choose some canonical parameters for our study as follows. Our two-dimensional Cartesian box is of size $x_m = 6, z_m = 2.5$ so that our convection zone (of depth unity) has an aspect ratio of 6, allowing plenty of room for convective cells, and so that the domain has plenty of room for overshooting. For purely hydrodynamic convection, we only solve equations 1, 2, 3 (under the ideal gas equation of state) as an initial value problem. Throughout this study, we canonically use $Ra = 4 \times 10^4$
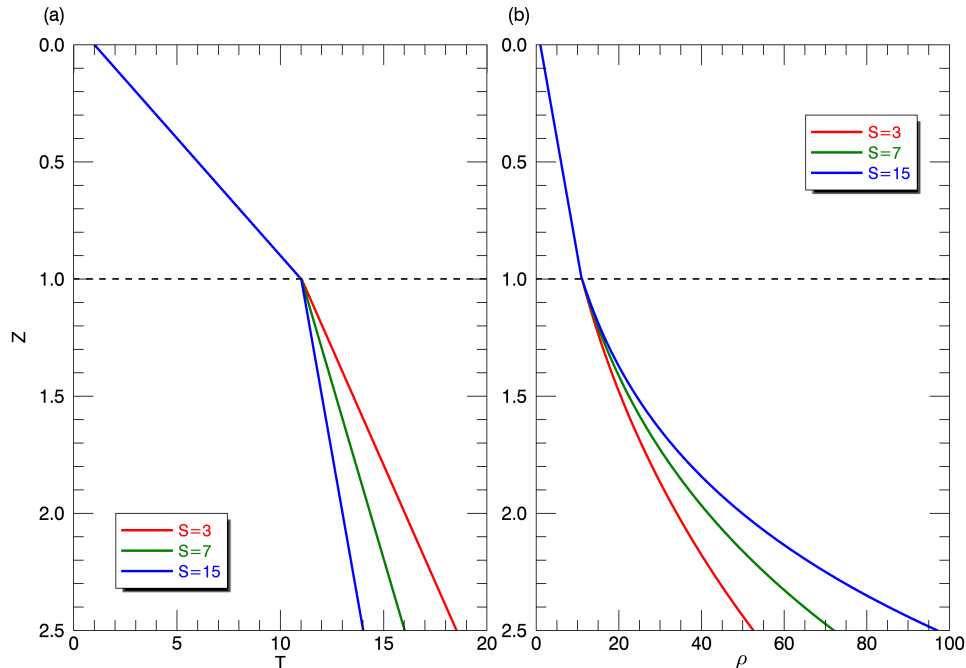
Figure 1. Profiles of polytropic thermodynamic initial conditions, a) T, and b) ρ, as a function of depth z at $x = 0$ for $S = 3$, 7 and 15. The dashed line marks the transition between the convection zone and the radiative zone.

and $Pr = 0.1$, in order to achieve reasonably super-critical dynamics at a Prandtl number less than unity. These values are in the correct regime for astrophysical purposes, but are orders of magnitude away from their true astrophysical values due to numerical limitations. We set the stratification using $m_1 = 1$ and $\theta = 10$ and choose S from the values $S = 3, 7, 15$. These choices of S provide a range of overshooting dynamics from deep to fairly confined, as we shall see shortly. For much of this paper, we use $S = 7$ as the canonical value, but all S are investigated and described in detail.

The time evolution of these equations from initial conditions consisting of a small amount of thermal noise in the convectively unstable layer sets up convection in the layer which can then overshoot into the lower convectively-stable layer. As an example, the time evolution of total kinetic energy in the simulation domain for the case with $S = 7$ is shown in Figure 2. An initial increase in the kinetic energy characterizes the formation of convection in the unstable layer, and, eventually, the kinetic energy settles to a statistical-steady (stationary) state.

Figure 3 shows snapshots of the vertical velocity (w) in the simulation domain at four different times during this evolution ($t \sim 24, 26, 71, 288$). We can see in Figure 3a that the initial evolution is marked by the formation of a cellular pattern of roughly five cells of convective motions, characterized by narrow downflows (blue) and broader upflows (red). As the convection ramps up,
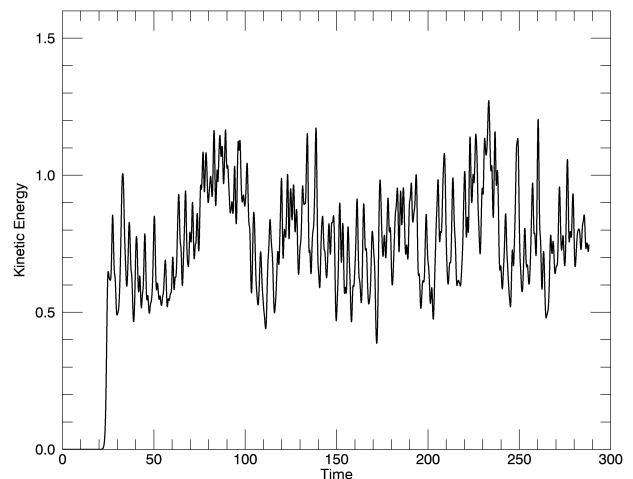
Figure 2. Kinetic energy as a function of time for the case with $S = 7$, $Ra = 4 \times 10^4$ and $Pr = 0.1$.

these more regular cellular patterns (probably related to the linear eigenfunctions) quickly evolve into more turbulent nonlinear dynamics, consisting of more time-dependent plumes that begin to overshoot into the stable layer below, as seen in Figure 3b. During the later, more characteristic, evolution, as shown in Figures 3c and d, plumes can form, migrate, split or merge, and the flows have established a strong identity in the stable layer, connected to the convective layer, as if there were
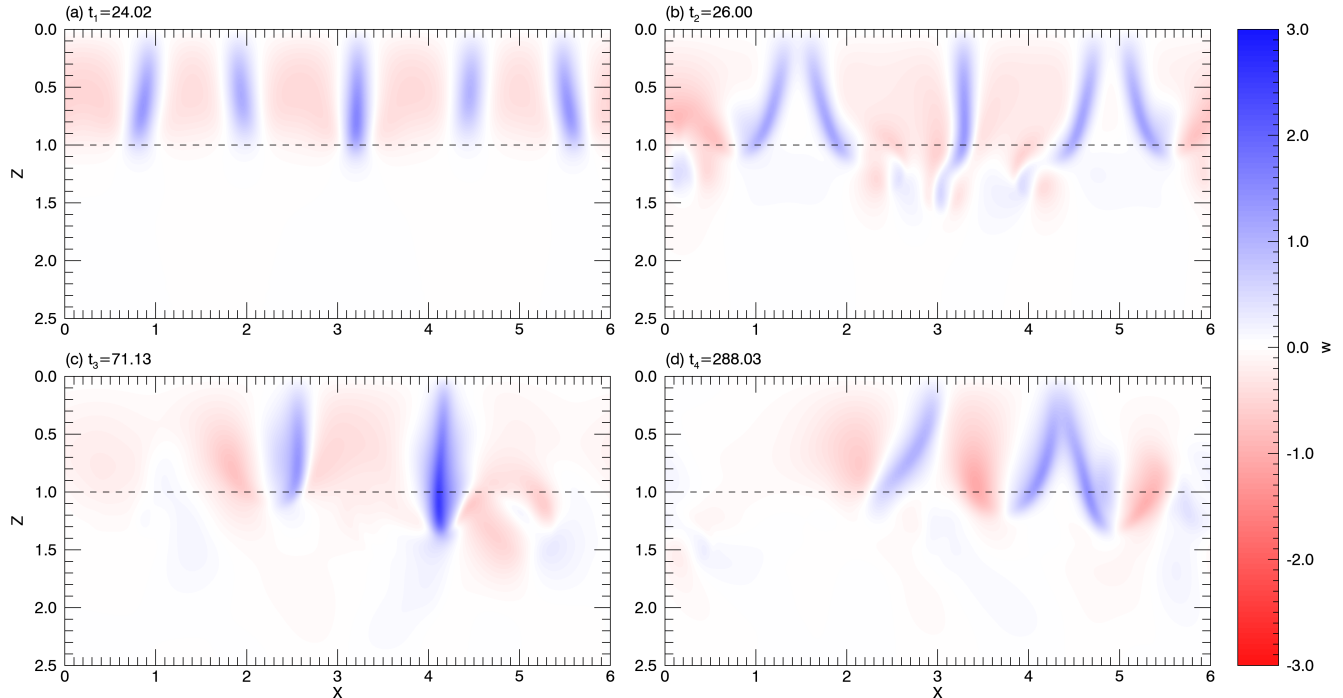
Figure 3. Vertical velocity (w) snapshots plotted at 4 different times for the case with $S = 7$, $Ra = 4 \times 10^4$ and $Pr = 0.1$. Blue color indicates downflows whereas upflows are red. The dashed line marks the transition between the convection zone and the radiative zone.

no boundary between the two regions, which is what we term "overshooting".

The depth to which this overshooting occurs is a topic of great interest in astrophysics and has been studied in detail in both 2D and 3D (e.g. Hurlburt et al. (1989, 1994); Brummell et al. (2002)). This overshooting depth depends on many of the parameters, Ra, Pr, S and its scaling with these parameters is of great interest to astrophysics, but here we concentrate on the effect of the the relative convective stability of the two layers, quantified by the parameter S (introduced by Hurlburt et al. (1994), defined in Section 2). Increasing S increases the relative stiffness of the stable layer since we have fixed the stratification of the upper layer. By "stiffness" here, we mean the resistance to convective motions entering the layer, in the sense of the buoyant deceleration. For greater S, due to the more rapid increase in density in the stable region (as can be seen in Figure 1), a plume entering this region feels a larger (negative) density perturbation and therefore decelerates more rapidly than it would at lower S.

The level to which the convection penetrates the stable region can be quantified by examining the time- and horizontally-averaged kinetic energy flux (over a representative time in the stationary state of the convection), as shown in Figure 6. The overshoot depth is often taken to be the depth at which the kinetic energy

has reached a fraction of its maximum value, typically 1% (e.g. Hurlburt et al. 1994; Brummell et al. 2002). This value reflects where, on average (both in time and space), the convective motions die out. Figure 6 shows this average kinetic energy profile for the three different values of S, ($S = 3$, $S = 7$, $S = 15$). We can clearly see that the overshoot depth decreases as S increases, as has been found many times before. The overshoot depths are $z_o = 2.08, 1.63, 1.55$ for $S = 3, 7, 15$ respectively. This result is an average over many instantaneous realizations, such as those shown as examples in Figure 4, which shows the vertical velocity (as for Figure 3) at a representative time in each of the $S = 3$ and $S = 15$ cases. In this Figure, it can clearly be seen that the dynamics are active much deeper in the stable layer for $S = 3$ (down to at least $z = 2$) and less deep (down to $z = 1.4$ or so) for $S = 15$, when compared to the case at $S = 7$ in the earlier figure. The scaling of the overshoot depth with S is of interest, but here we are more concerned with creating initial conditions for the later parts of our study.

We add a quick note regarding "overshooting" convection versus "penetrative" convection. If the dynamics in the overshoot layer below the convection zone are sufficiently energetic to mix the stable region strongly, driving it towards a well-mixed adiabatic system with a constant entropy, then the "overshooting convection" be-
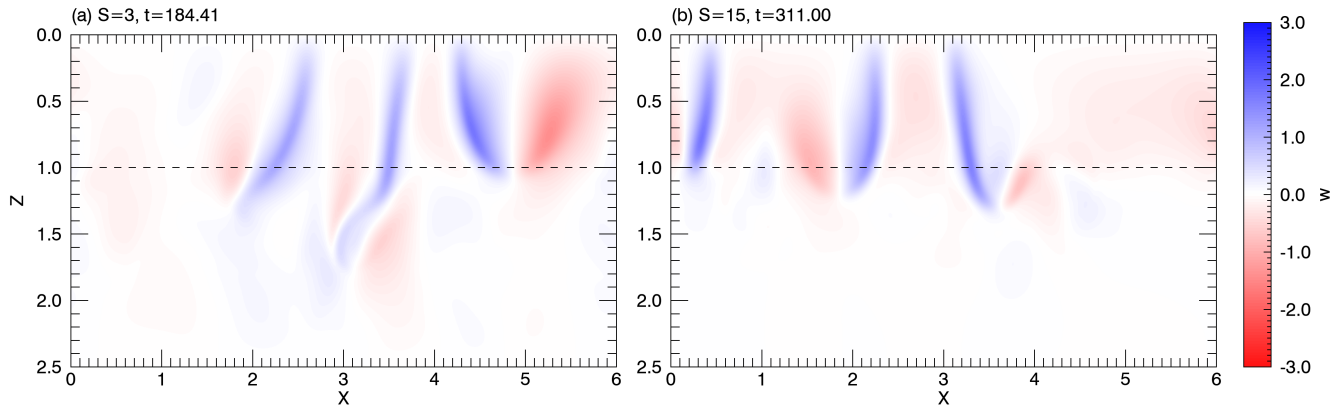
Figure 4. Vertical velocity (w) snapshots for (a) $S = 3$ and (b) $S = 15$.
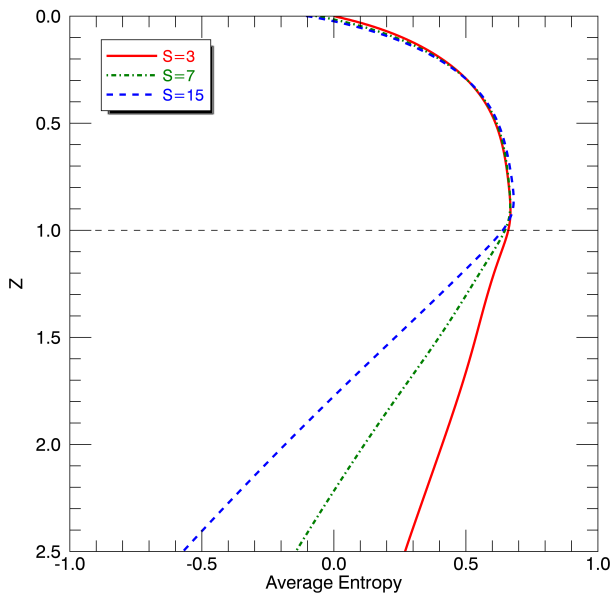
Figure 5. Time- and horizontally-averaged entropy as a function of height for $S = 3$, 7, and 15.

Figure 6. Time- and horizontally-averaged kinetic energy flux as a function of z for three different cases, $S = 3$, 7, and 15. The horizontal dashed line at $z = 1$ marks the transition between the convection zone and the radiative zone. Overshooting depth is the z-location at which the curves meet the y-axis in the stable region.

comes known as "penetrative convection" (Zahn 1991). All our cases here are overshooting convection and not penetrative convection. Figure 5 shows the time-averaged entropy for the three cases. We can see that significant mixing has not occurred below the convection zone, since there is still a strong entropy gradient below $z = 1$.

3.2. *Rise of Flux tubes in Pure Convection*

Having established a purely convective background state, we now wish to understand under what conditions a flux tube is able to rise through such a state in the absence of any large-scale volume-filling field. We need to do this since we are interested in effects on the flux tubes that would otherwise emerge buoyantly at the

top of the convection zone. We therefore now turn to MHD simulations where we add an *isolated* flux tube to established convection. Again, similar simulations have been performed before, for example, in 3D for fully compressible and anelastic convection Cline (2003); Abbett et al. (2004). A discovery of this past work has been that magnetic structures need to possess magnetic energy greater than the peak kinetic energy of the flow to survive transit of the convection zone. Here, we need to establish exact values for our particular setup to inform later, more complete and complex simulations including a large-scale background field.

The initial setup for these cases consists of an instance in time from the stationary state of one of the overshooting convection simulations, such as those in Figures 3c,d or 4). To this state, we add a twisted magnetic flux tube embedded at a chosen location in the stable zone (see, for example, Figure 7a or 8a). The total magnetic field of the flux tube is given by

$$\mathbf{B} = (B_x, B_y, B_z) = \mathbf{B}_{\text{tube}} =$$
$$\left(-2q\frac{(z_c - z)}{r_o}, 1 - \frac{r^2}{r_o^2}, -2q\frac{(x - x_c)}{r_o} \right)$$
$$\text{for } r \leq r_o \quad (15)$$

where q is the initial twist of the field, x_c and z_c are the horizontal and vertical locations of the center of the flux tube, r_o is the outer radius of the structure, and $r = ((x - x_c)^2 + (z - z_c)^2)^{1/2}$ is the cylindrical radius measured from the center of the tube. Note that the field is purely axial at the center of the flux tube and the amplitude there is unity. With $|q| = 0.5$, the azimuthal field in the tube is unity at $r = r_0$. We only examine $|q| = 0.5$ in this study, and in this Section of the work, the sign of q does not matter, since there is no background field against which its orientation can be judged. We choose $x_c = 3, z_c = 2$ as the standard initial location, and we adopt $\zeta = 0.001$ from now. The latter value is small so that tubes, which can have strong gradients at the edges, do not diffuse too quickly, i.e. other dynamical times of interest, like the buoyant rise time, are quicker than the time to diffuse the flux tube magnetic perturbation. This value renders the magnetic Prandlt number $Pm = \sigma/\zeta = 100$ which is not representative of astrophysical values that are typically less than one. This is a statement that our simulations are too viscous and therefore not as turbulent as they should be, but this is a numerical limitation. At this point, we only examine $S = 7$ and leave the study of the effects of varying S later.

The canonical set of governing parameters is therefore now $S = 7, Ra = 4 \times 10^4, Pr = 0.1, \zeta = 0.001$. We are left to vary the Chandrasekhar number, Q, as the key parameter of interest. With unit maximum amplitude of both the axial and azimuthal fields of the flux tube, the Chandrasekhar number entirely determines the initial strength of the magnetic field (in this case, the flux tube) and determines the dynamical influence (via α) of the Lorentz force (see equation 2). When we add the flux tube to the existing fields, we do so assuming that the total pressure and the temperature equilibrate quickly, so that the increase in magnetic pressure is entirely compensated for by a drop in density. This means

that the initial condition is not in equilibrium and the tube experiences an initial upwards buoyancy force.

Figure 7 shows the evolution of the full set of Equations 1-6 for such an initial state. This Figure shows intensity plots of the normalized axial field, B_y, which is a good indicator of the location of the tube, overplotted with the normalized vertical velocity, w, representing the convective flows. We use the absolute maximum values of B_y and w as the normalizing factors for the axial field and vertical velocity, respectively. The case shown is at the canonical parameters, for a positively-twisted flux tube with $Q = 2 \times 10^8$, and the Figure displays four different times. Figure 7a shows the initial location of the cylindrical flux tube at $(x_c, z_c) = (3.0, 2.0)$ deep in the stable region, along with the overshooting convective motions. Here, red and blue colors indicate upflows and downflows respectively. As the flux tube starts rising due to its magnetic buoyancy, the initial rise is reasonably symmetric, and quickly becomes accompanied by the formation of vortices, a characteristic reminiscent of non-convective flux tube rise (Fig. 7b). The impact of overshooting convection on the dynamics of the flux tube is minimal at this stage. As the flux tube enters the overshooting region ($0 \leq z \leq 1.5$) and gets closer to the transition between the stable and convective layer, the effect of convective motions becomes evident on the flux tube. Figure 7c shows that the flux tube is located beneath a downflow. The symmetric rise of the flux tube is broken, as buoyant and advective forces act on the tube, and the driving vortices are stretched. However, due to sufficient initial twist ($|q| = 0.5$) and sufficient buoyant ($\propto Q$), the flux tube maintains coherency and navigates its way into an upflow and thereby to the top of the convective simulation domain (Fig. 7d). We consider these dynamics as a successful rise of the flux tube (but will develop a more quantitative measure later)

Figure 8 represents a case similar to Figure 7 but for a lower Q. The simulation starts from the same initial steady-state convection and initial magnetic profile, albeit now with $Q = 5 \times 10^6$ (Figure 8a). With a weak buoyancy perturbation due to lower Q, the initial rise of the flux tube is very slow. Figure 8b shows that the flux tube barely rises in the stable zone with no distinct vortices forming. The slow rise brings the tube to the edge of the overshooting region ($z \sim 1.5$ where even these weak flows distort the cylindrical flux structure (Fig. 8c). Eventually, other forces dominate over buoyancy and the flux tube gets stretched, and its rise is halted (Figure 8d). We consider this is an example of an unsuccessful rise of the flux tube. Even with minimal interaction with the overshooting, the buoyancy was insufficient to enable a rise.
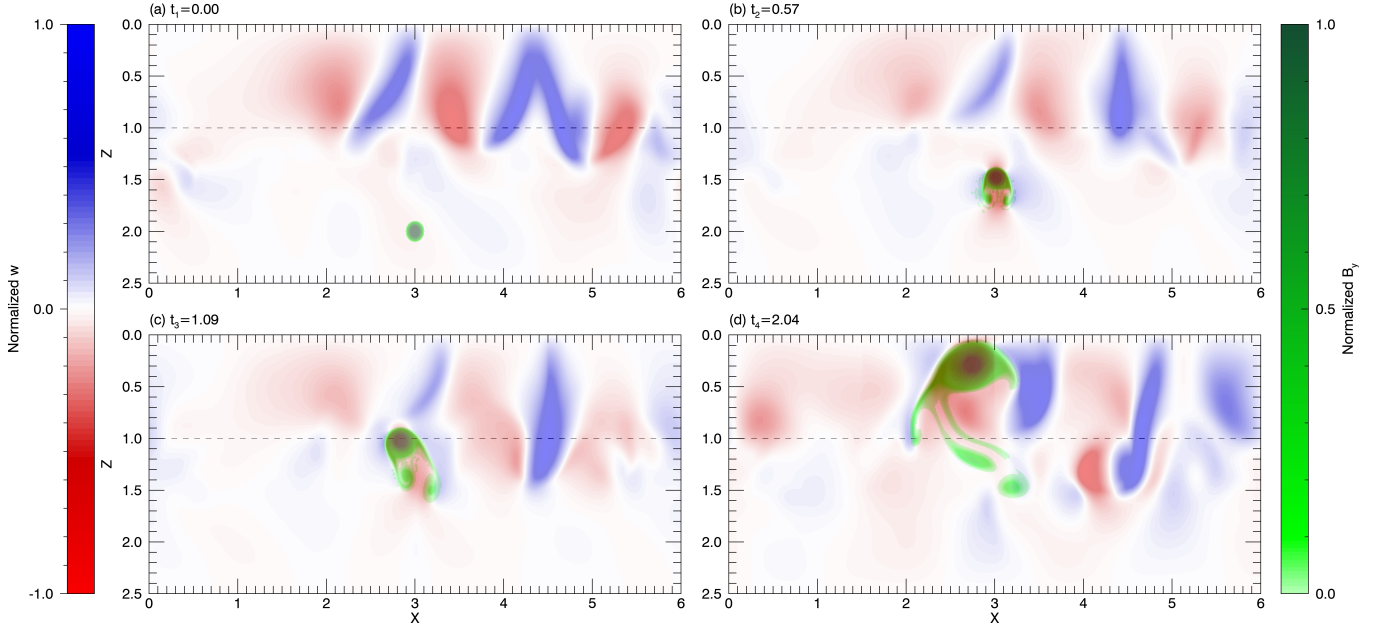
Figure 7. Intensity plots of normalized B_y, overplotted with the normalized vertical velocity, w, as a function of time for the case with $S = 7$, $Ra = 4 \times 10^4$, $Q = 2 \times 10^8$, $Pr = 0.1$ and $Pm = 100$. The initial location of the flux tube is $(x_c, z_c) = (3.0, 2.0)$. The dashed horizontal line indicates the transition between the convection zone and the radiative zone.
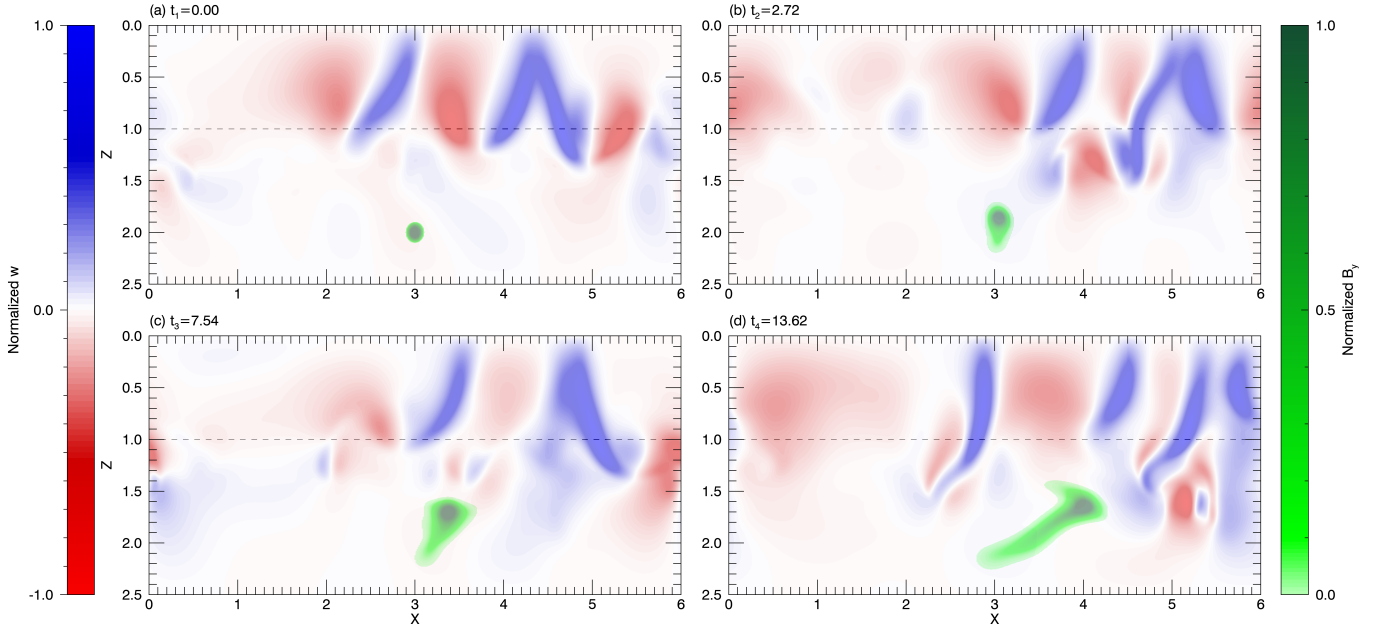
Figure 8. Same as Figure 7 but for $Q = 5 \times 10^6$.

It is reasonable then, in this study, to conclude that the rise or non-rise of the flux tube is determined by the amount of buoyancy (controlled by Q) imparted to the flux tube (for fixed other parameters). We now explore a wider range of Q to understand this dependence in more detail. To determine the ultimate fate of a flux tube more concisely, we turn to a more quantitative and explicit measure of the rise characteristics, denoted by $z_{ft}(t)$, that tracks the z-location of the maximum of the axial field, B_y, as a function of time. From Figures 7 and 8, it is clear that this quantity tracks the progress of a tube reasonably well.

Figure 9 shows $z_{ft}(t)$ for a range of simulations that were initiated identically but for varying Q. A relatively lower Q leads to an almost neutrally buoyant flux tube that does not rise and remains embedded in the stable zone ($Q = 5 \times 10^6, 1 \times 10^7$; red and green markers). A relatively middling value of Q, for example, $Q = 4 \times 10^7$ (blue markers) leads to a slow rise of the flux tube through the stable zone and into the convection zone, where it experiences some substantial variations due to interactions with upflows and downflows but nevertheless rises. With higher Q values, the flux tube rises quickly through the both the stable zone and the convection zone to the top of the domain (e.g. $Q = 8 \times 10^7, 2 \times 10^8$; magenta and black markers). In this plot, the black marker corresponds to the $Q = 2 \times 10^8$ case discussed in Figure 7 and the red marker corresponds to the $Q = 5 \times 10^6$ in Figure 8. Note that we curtail such plots, stopping following the tube either after it reaches the top of the simulation domain or when it has become clear that a tube has stopped rising.

From this information, we choose to use $Q = 2 \times 10^8$ as the value of Q for our canonical set of parameters used in the next sections. Our aim is to evaluate the effect of the sign of twist in conjunction with a large-scale background field on emergent tubes. This case provides a clear and definite emergence in the absence of such effects. It can be interesting to examine other cases too, and this will be done later in this paper when examining different S.

At this point, it is important to realize that here the sign of the twist of the flux tube does not make a difference to the dynamics. The evolution and fate of a positively-twisted flux tube and a negatively-twisted flux tube inserted into convection without any background field is the same. This is illustrated by Figure 10) which shows $z_f t$ for two tubes with opposite signs (panel a), and a snapshot of the simulation at a late stage for a negatively-twisted tube which can be compared with that shown for a positively-twisted tube in Figure 7d. Clearly, the dynamics are very similar, and
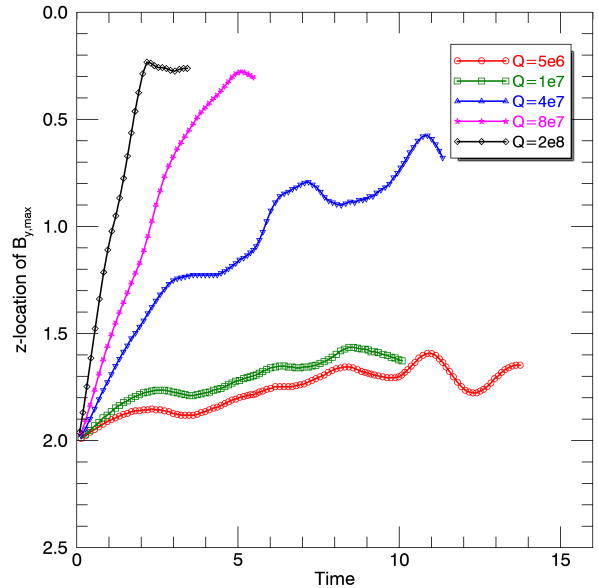
Figure 9. The maximum of B_y as a function of time z_{ft} for different Q. Other parameters are $Ra = 4 \times 10^4$, $Pr = 0.1$, $\zeta = 0.001$, $q = 0.5$, and $S = 7$.

the twist serves mainly to maintain the coherence of the tube. We will show that this symmetry is broken by the inclusion of a background field in later sections of this paper.

3.3. *Dynamical formation of Background Magnetic Field*

Papers 1 and 2 explored the effect of a background magnetic field on the rise of flux tubes by artificially imposing the background field as a function that decreased exponentially with height. The authors of those papers argued that the turbulent convective pumping of large-scale magnetic fields (see e.g Tobias et al. 2001b) would likely achieve some profile of the background field where the majority of the field was confined below the convection zone. The exponential profile was their attempt at a simple model of part of this profile. In this section of this paper, as part of the setup of our initial state for the ultimate simulations, we explore the self-consistent formation of a large-scale background magnetic layer by magnetic pumping due to the presence of the overshooting turbulent convection, instead of assuming its existence, as in the previous work. Again, simulations of this type have been performed before (see e.g Tobias et al. 2001b) and transport of magnetic field out of convection zone into a stable layer down a gradient of turbulent intensity is fairly well-understood. Our aim here is simply to create self-consistent initial conditions for the large-scale background field, rather than
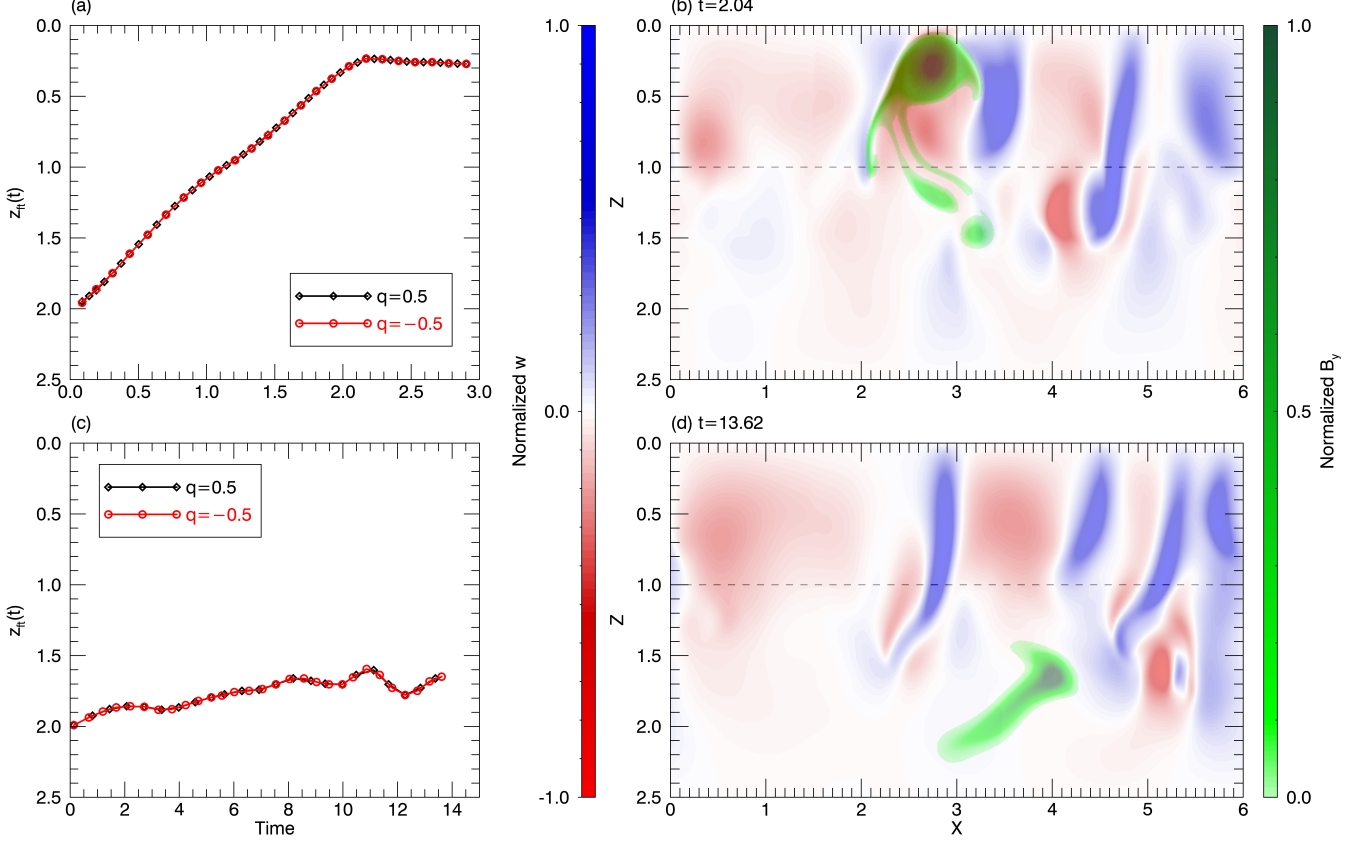
Figure 10. Comparison of the dynamics of positively- and negatively-twisted tubes for $Q = 2 \times 10^8$ (a and b) and $Q = 4 \times 10^6$ (c and d): (a) z_{ft} plotted as a function of time for both $q = 0.5$ and $q = -0.5$, (b) The equivalent of Figure 7d but for $q = -0.5$, (c) z_{ft} plotted as a function of time for both $q = 0.5$ and $q = -0.5$, (d) The equivalent of Figure 8d but for $q = -0.5$.

artificial ones. Since the selection mechanism discovered in Papers 1 and 2 depends on the relative strengths of the tube and the background field, our goal here is to be able to control the amplitude of the profile of the pumped field to explore this relationship.

We start with a steady-state pure convection solution from Section 3.1 and impose a thin horizontal magnetic layer concentrated in the convection zone. Note that, in this Section, no flux tube is imposed. The magnetic layer is given by

$$\mathbf{B} = (B_x, B_y, B_z) = \mathbf{B}_{\text{layer}} =$$

$$\left(\tanh\left(\frac{z - z_{bot}}{\delta}\right)\tanh\left(\frac{z_{top} - z}{\delta}\right), 0, 0\right)$$

$$\text{for } z_{bot} \leq z \leq z_{top} \quad (16)$$

where z_{top} and z_{bot} are the top and bottom location of the layer respectively, and δ is the smoothing width of the edges of the layer. For a standard initial condition, we use a layer where $z_{bot} = 0.80, z_{top} = 0.75$ and $\delta = 0.01$. The other parameters remain at the canonical

values ($Ra = 4 \times 10^4$, $Pr = 0.1$, and $\zeta = 0.001$) and we can again choose Q to determine the initial strength of the magnetic layer. This, in turn, affects the initial magnetic buoyancy of the layer, since we again adjust the background thermodynamic state to maintain total pressure and temperature equilibrium, as in the previous section. We have experimented with omitting the thermodynamic adjustment to avoid certain numerical issues, and found that this makes little difference, since the code adjust pressure balance very quickly.

The choice of Q is a little complicated for the following reasons. In Section 3.2, we established that a flux tube with $Q = 2 \times 10^8$ rises through the convection and therefore we will need to run our ultimate simulations (involving both flux tubes and background field) at this Q value. The work of Paper 2 showed that the key factor in the selection mechanism was the relative values (and orientation) of the azimuthal field in the tube and the background field strength. The former is initially dictated by q and can be different from the axial field strength of unity. However, our choice of $|q| = 0.5$ makes

the peak azimuthal field also conveniently equal to unity, and therefore, both of these quantities are governed by the value of Q. However, we wish to be able to control the relative strengths of the azimuthal field in the tube and the background field in order to explore the regimes of Paper 2. From that previous work, we expect the background field strength to be between roughly 5% – 20% of the tube strength for the selection mechanism of Papers 1 and 2 to manifest. We therefore need to be able change either the resultant azimuthal field strength or the resultant background field strength at a fixed Q to be able to realize this ratio. We could achieve this by varying $|q|$, but instead we choose to control the resultant strength of the evolved background field (in order to avoid having to repeat the simulations of the previous section many times). This is not particularly artificial, since any pumping calculation with the magnetic boundary conditions specified (Equation 2) runs down anyway, so that the magnetic field amplitude decreases from unity to some significantly lower value. Changing the initial layer amplitude allows any chosen final amplitude to be realized. In essence, there is an effective Q of this run-down state that we can control, given by the square of the amplitude of the state times the original Q: $Q_{\text{eff}} = Q|\mathbf{B}|^2$.

With this in mind, we purposely start our pumping simulations with a lower Q ($= 4 \times 10^6$) in this setup. This allows a two-fold flexibility. Firstly, at large Q, strong field can quickly accumulate at the upper boundary causing numerical problems; lower initial Q can avert this unphysical issue. Secondly, after evolving the system at lower Q, we can evaluate the peak amplitude of the final horizontally-averaged profile, and then scale this state to whatever peak amplitude we desire, essentially adjusting the Q_{eff}. We can then take this as an initial condition, and run at the higher Q (the canonical Q that we must use when a tube is eventually present in the next Section) until it relaxes into the pumped state for that value. This process is equivalent to running at different amplitudes of the initial layer at fixed Q (and therefore different Q_{eff}) but allows us to have fast access to a pumped state with a controllable peak amplitude of the profile.

We illustrate this whole process with Figures 11 and 12. Figure 11 gives a good impression of the magnetic pumping process by showing snapshots of the horizontal magnetic field B_x (normalized by its maximum) as a function of time in the simulation at the canonical parameters. The initial magnetic layer can clearly be seen in Figure 11a. Panel b exhibits the early evolution of the layer, showing that these are dominated by the competing effects of magnetic buoyancy and downward

transport of flux caused by advection in the convective plumes. Some sections of the layer rise by the combined effects of the magnetic buoyancy of the layer and upflow advection, whereas some sections get dragged towards and into the stable layer, in strong downflows where advection overcomes the buoyancy. After this initial adjustment, the advective churning of the field dominates, as can be seen in panels c-d. At this stage, the small-scale turbulent interactions with the magnetic field dominate, leading to the turbulent transport mechanism of magnetic pumping. The overshooting convective motions therefore transport magnetic flux to the stable region, as seen in Figure 11e-f. The pumped fields slowly accumulate at the edge of the overshoot region, where their residual magnetic buoyancy is balanced by the pumping mechanism.

In panels g-h of Figure 11, we show an example of the adjustment of the peak amplitude of pumped field. We evaluate the peak strength of the current pumped layer by calculating a time average of the horizontal field. Due to the influence of magnetic diffusion and vertical boundary conditions, the peak strength of the pumped layer has diminished considerably from the initial value of unity. We re-scale the magnetic fields in the whole simulation domain by a chosen scaling factor. If required, we can also adjust the Chandrasekhar number of the simulation at this point to the canonical value of $Q = 2 \times 10^8$. We then further evolve the new system, treating the scaled magnetic field as a new initial condition, over many convective turnover times. This allows the system to relax to a new dynamically-consistent pumped magnetic layer, as shown in Figure 11g-h.

It should be noted that even though the pumped magnetic layer in Figure 11h (for example) looks fairly smooth, thanks to the considerably higher value now of the peak in the pumped layer, there are considerable local variations if we check the vertical profiles of the layer at different horizontal locations. In Papers 1 and 2, the artificially-imposed background field was uniform in the horizontal direction, whereas here, the self-consistently generated pumped field state is not. In order to make contact between the two different works, we here calculate (and use for comparison) the time- and horizontal-average of the horizontal magnetic field B_x. First, we show as Figure 11 the time evolution of the horizontally-averaged field for various stages in the calculation shown in the previous Figure. For each time portion, the initial and final state is shown as a thicker line, and the thinner lines show regular time intervals between these end points. Panel a again shows the initial dynamics where the profile evolves from the initial layer located between

$z = [0.7, 0.8]$. Initially, it can be seen that the profile relaxes in shape and amplitude somewhat, and moves upwards due to magnetic buoyancy and starts to accumulate at the top. At the same time, some of the average field gets moved towards the lower stable layer, creating a second accumulation peaked at around $z = 1.4$. In panel b, later in time, we see that on average, the field starts to be evacuated from the upper boundary and the interior of the convection zone. The peak around $z = 1.4$ becomes (relatively) more prominent, but also a second peak around $z = 1.8$ starts to form, just below the overshoot region. This latter peak is the progenitor of the pumped layer, as can be seen in panel c, where, as time progresses, this peak becomes the dominant dynamical feature in the average field. Panel d shows how we control the amplitude of the pumped field. Here, we have taken the end result of the earlier calculations, and rescaled the pumped field by a chosen factor (a factor of 20 in this case) and continued the evolution. It can be seen that this achieves a stable profile of pumped field on average, with a peak amplitude of about 0.2. This type of state is what we desire as an initial condition for later calculations also containing a flux tube with peak field amplitude of unity. Such a profile provides the ratio of amplitudes where the background field is at about peak amplitude of 20% of the tube peak amplitude. It should be noted that pumped profile can still evolve and run down due to the magnetic boundary conditions. However, this evolution is in general very slow compared to other dynamics that we are interested in (such as the rise time of a flux tube) and therefore can be considered essentially steady. As can be seen in panel d, this is because the profile can evolve such that there are no gradients of the (average) field at the boundary (especially at higher S than is shown in this case: see later) and/or the profile becomes essentially piecewise linear with very little diffusion acting (except at the junctions of the piecewise profile).

Figure 13 shows the final time- and horizontally-average state of the pumped field as a function of height at the canonical parameters with $Q = 2 \times 10^8$. This is the state that we will use for the next Section. The peak strength of this pumped layer is about 0.21, or 21%, compared to a unit strength flux tube. The filled-diamond markers are placed to indicate the locations where the average field strength is 1, 2.5, 5, 10, 15, and 20% on the upslope section of the pumped layer. We will use these locations from this layer in the next Section.

3.4. *Rise of Flux tubes in the presence of a Background Field*

We now come to the main point of this paper and examine the dynamics of the rise of magnetic flux tubes in the presence of convection and a background magnetic field. We take the setup we arrived at in Section 3.3, where we have statistically steady-state convection with a self-consistent magnetic field in the form of a layer in the stable zone. To this we introduce a flux tube. The total magnetic field is then given by

$$\mathbf{B} = (B_x, B_y, B_z) = \mathbf{B_{tube}} + \mathbf{B_{pumped}} \qquad (17)$$

where $\mathbf{B_{tube}}$ is the field of a tube as in Equation 15 and $\mathbf{B_{pumped}}$ is the field resultant from the end of the simulations in the previous Section 3.3. In this Section, we consider flux tubes with both positive (anticlockwise) and negative (clockwise) twist, q, with a fixed magnitude $|q| = 0.5$. The other parameters are the canonical set: $Ra = 4 \times 10^4$, $Pr = 0.1$, $\zeta = 0.001, S = 7$ and $Q = 2 \times 10^8$.

There are a few important points to note at this stage. Firstly, introducing a flux tube, $\mathbf{B_{tube}}$, again requires a thermodynamic perturbation in the background stratification for consistency, as in the case when there was no large-scale background magnetic field already present. As before, we choose to adjust the density whilst maintaining the current temperature in the tube. This imparts an initial magnetic buoyancy to the tube, as was the case in the absence of a background magnetic field. The pumped layer, $\mathbf{B_{pumped}}$, is already dynamically consistent with the background stratification (see Section 3.3) and the thermodynamics do not need to be adjusted for this component.

Secondly, as determined in detail in Paper 2, the relative strengths of the twist of the tube and the background field are the key determining factors in the differential evolution of differently twisted flux tubes. Here, we have fixed the strength of the tube (via its unit maximum axial field strength and fixed twist value, q) and are left with two controls over the relative strength of the background field. One control is that we can adjust the peak amplitude of the pumped layer as described in the previous section. The other control is that, even for a given peak amplitude in the initial condition for $\mathbf{B_{pumped}}$, we can adjust the depth at which the flux tube is introduced, thereby determining both the background field value that the tube experiences initially and the amount of pumped background field the tube experiences during transit upwards.

Our strategy here initially is to select a case from the previous section where the peak amplitude of $\mathbf{B_{pumped}}$ lies in realm where Paper 2 predicted that a selection mechanism may occur. We then select particular depths at which the flux tube is introduced into the pumped
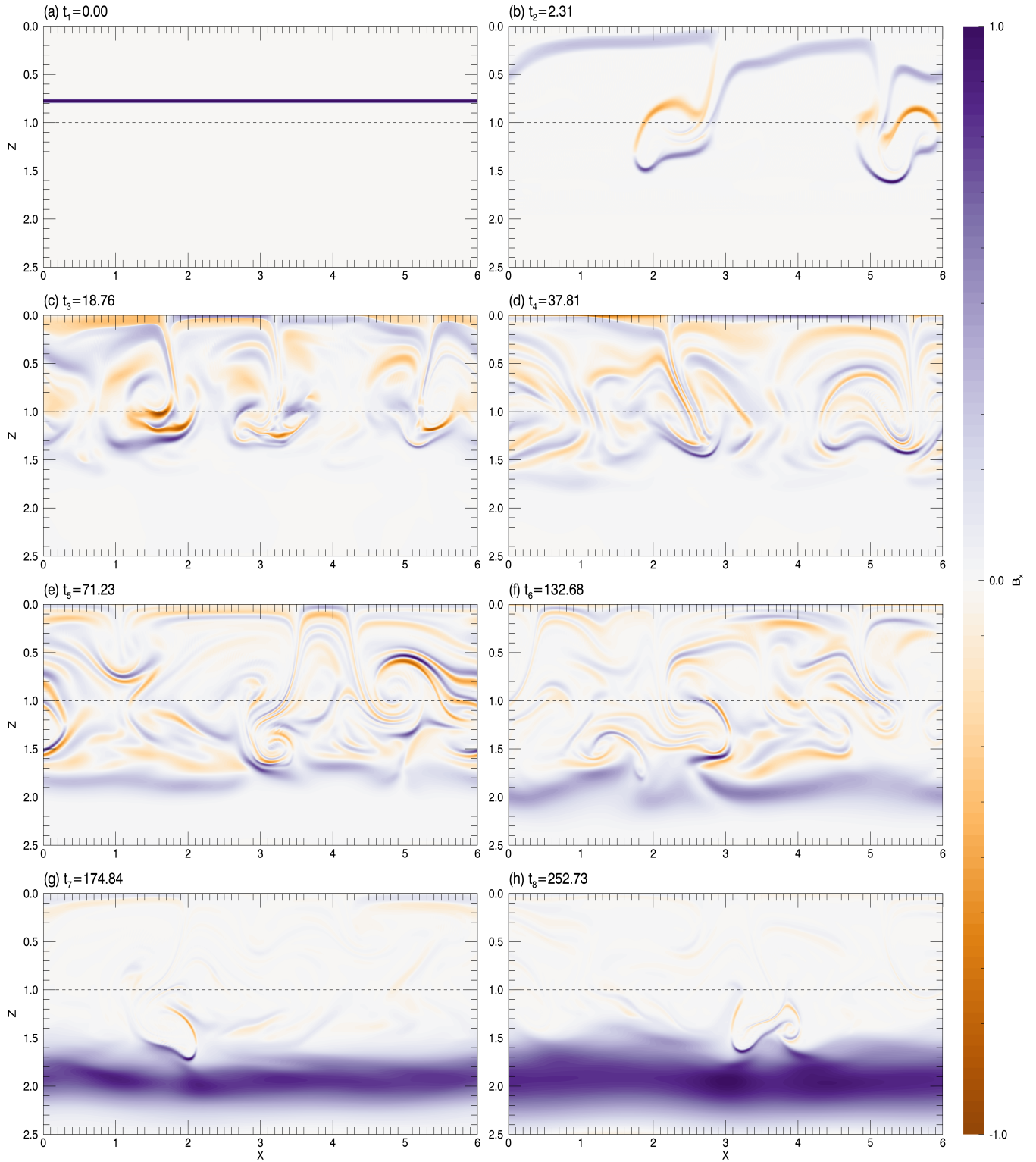
Figure 11. Snapshots of normalized horizontal magnetic field, B_x, as a function of time. (a)-(f) have $Q = 4 \times 10^6$ whereas (g)-(h) have $Q = 2 \times 10^8$.
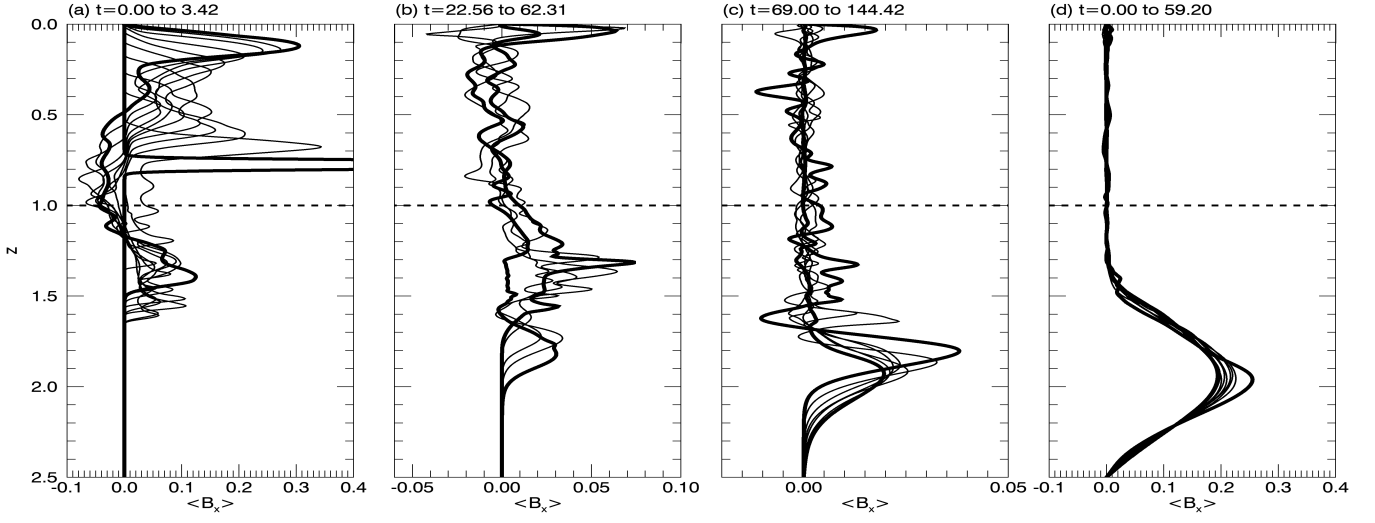
Figure 12. Time- and horizontally-averaged pumped horizontal field as a function of height (z) for the case with $S = 7$. Initial and final profiles are plotted with a thicker line in each of the subplots. (a) shows the initial pumping of the imposed magnetic layer. The final profile of the pumped field is multiplied by a factor of 20 and its evolution is shown in (d).
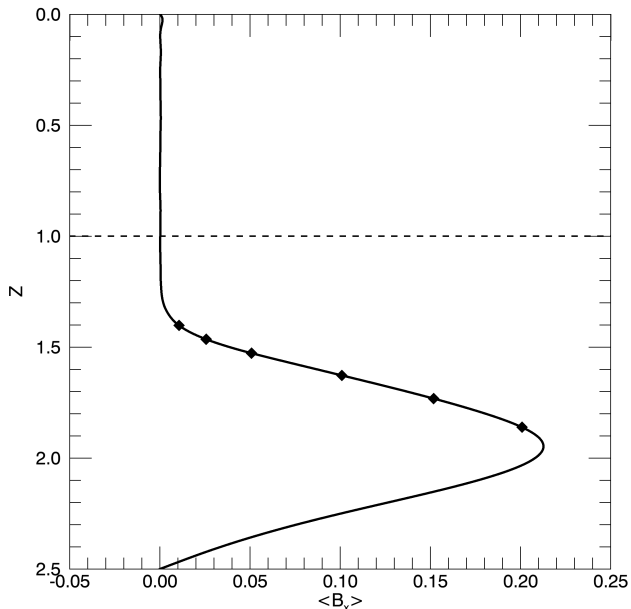
Figure 13. Time averaged pumped horizontal field as a function of height (z) for the case with $S = 7$. Black diamond markers indicate the different z-coordinates centred at which flux tubes are introduced. These z-coordinates correspond to 1, 2.5, 5, 10, 15 and 20% strength of the pumped horizontal field as compared to the flux tube strength. The dashed line marks the transition between the convection zone and the radiative zone.

magnetic layer in order to vary the precise ratio of the twist field in the tube to the averaged pumped field strength (see diamond markers in Fig. 13). We investigate the details of varying the peak amplitude and related local effects later. We initially choose all the locations of the introduction of the flux tube to be on the upper side of the pumped layer. We do this because we assume that flux tubes are likely to be formed by magnetic buoyancy instabilities, which require that the magnetic field increases sufficiently strongly downwards, therefore the most likely initiation of tubes is on the upper side of the pumped layer. We argue also that, while flux tubes may perhaps form below the peak of the pumped magnetic layer, the eventual rise of such tubes is more likely to fail completely due to the significant extent of the strong magnetic field that it has to rise through, and that failed cases are less interesting to us initially. We adopt the notation that, for example, $B_s = 0.10$ corresponds to a time-averaged pumped background field strength (at the depth of the center of the tube) that is 10% of the unit peak strength flux tube (in both axial and, more importantly, azimuthal field). Locating the flux tube at the vertical position

corresponding to this strength in the average pumped field is now one of our key control parameters.

Figure 14 shows intensity plots of normalized B_y (green color scale), overplotted with normalized vertical velocity, w (red-blue color scale), for both a positively-twisted (panel a) and negatively-twisted (panel b) flux tube for four different times in the evolution of the system. Here the red and the blue color represents upwards and downwards vertical velocity respectively. For this case, the flux tube in both cases is introduced at a depth such that $B_s = 0.10$ as explained above. Figures 14a and b therefore look identical, with the flux tube embedded between two convective downflow plumes. However, the dynamics subsequently evolve substantially differently in the two cases.

The flux tube with a positive twist rises initially due to its imposed magnetic buoyancy, as in the case with no background field. However, the rise this time is not entirely coherent as the flux tube is rising through the pumped horizontal background field. Instead, as the tube rise, it experiences some axial flux loss along the background field B_x accompanied by substantial disruption of the vortices that form in the isolated tube case. This can be seen qualitatively but clearly in Figure 14a at $t_2 = 0.81$. These effects, due to the presence of the background field, were also seen and described in Papers 1 and 2. Furthermore, the flux tube in this case is located between two merging downflows at these early stages in the plots. However, even with all these relatively unfavorable circumstances for its rise, the flux tube successfully enters the convectively unstable layer (Fig. 14a at $t_3 = 1.35$) and eventually rises to the top in a weak upflow next to the strong merged downflow (Fig. 14a at $t_4 = 2.29$). Note that the effect of convective motions on the rise is immediately evident as the flux tube does not rise symmetrically (about the line $x = 3$) and so these simulations are clearly distinct from those of Papers 1 and 2.

In stark contrast, the dynamics of the flux tube with a negative twist are entirely different. Figure 14b at $t_2 = 0.24$ shows that, in the presence of the background field, the flux tube does not even begin to rise through the convective background. The flux tube structure simply gets distorted quickly and breaks apart, with axial flux rapidly drained along the B_x fieldlines (see Fig. 14b at t_3 and t_4).

At this point, we have already arrived at an important conclusion that parallels those of Papers 1 and 2, i.e. that the flux tube dynamics in the presence of a background field are very different compared to cases where there was no background field present. With no background field, tubes of both twists rose similarly, with the
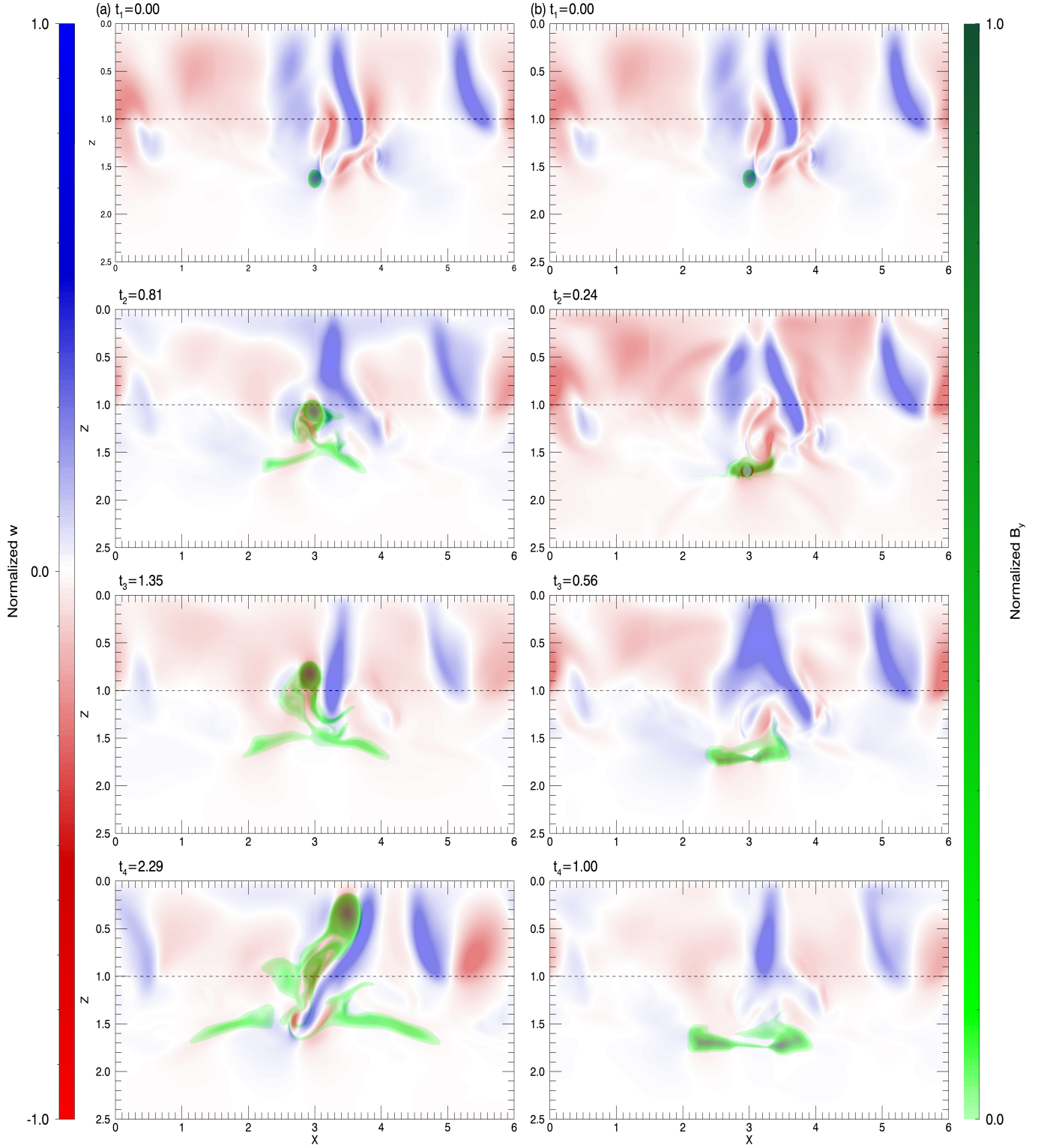
Figure 14. Intensity plots of normalized B_y, overplotted with normalized vertical velocity, w, for (a) $q = 0.5$ and (b) $q = -0.5$ at four different times. The time-averaged pumped background field strength, B_s, at the center of flux tube in both cases is 0.10, i.e., 10% of the initial strength of the flux tube.

dynamics dominated by their identical magnetic buoy-ancy (see Section 3.2), whereas, here, in the presence of background fields, positively- and negatively-twisted tubes evolve very differently. In these new simulations, these conclusions, that are similar to those of Paper 1 and 2, are reached despite the presence of convection and a more self-consistent background field. Put in a slightly different way, we have shown that a positively-twisted flux tube is more likely to rise than a negatively-twisted tube in the presence of convection and a self-consistently pumped background field of strength, $B_s = 0.10$. Since the magnetic buoyancy forces exerted by both signs of twist are identical, we attribute these effects to mag-netic tension effects, as described in Papers 1 and 2, even though this system is more complex. We examine this quickly with the Figure 15 and investigate this in more detail later. Figure 15 shows the vertical profile of the vertical tension force $F_{z,tens} = (B_x\partial_x + B_z\partial_z)B_z$ on the $x = 3$ line through the center of the tube at $t = 0$, corresponding to the state in panels a and b in Fig-ure 14. These line plots confirm that, compared to the case where no background field is present (dashed line), the positively-twisted tube has enhanced negative (up-ward) tension in the lower half of the tube, whereas the negatively-twisted tube has enhanced positive (down-ward) tension in the upper half of the structure. In the former case, the tension acts in concert with the buoy-ancy force, helping the rise of the tube, whereas in the latter case, tension acts against buoyancy, decreasing the chances of rise. This is the case despite the fact that the background pumped field may have significant variations away from the mean profile at this particular location.

4. CONCLUSION

In this paper, via a series of numerical simulations, we have clearly established an asymmetry between the buoyant rise of oppositely twisted flux tubes when in the presence of overshooting convection and a dynamically-formed large-scale background field. Specifically, we find that a positively-twisted (anticlockwise) flux tube is more likely to rise than a negatively-twisted (clock-wise) tube when the rise is in the presence of a pumped field that is, on average, oriented horizontally in the pos-itive direction. This result affirms the existence of a se-lection mechanism based on tension effects akin to the non-convective case described in Papers 1 and 2. This mechanism operates because of the relative orientations of the azimuthal field of the tube and the horizontal background field. For a positively-oriented background field, the azimuthal field of a positively-twisted flux tube is enhanced on the lower side and reduced on the up-
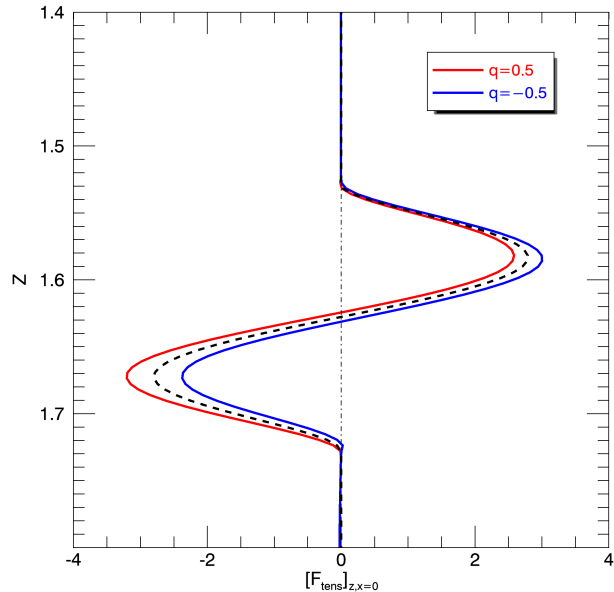
Figure 15. Plots from the canonical case at $S = 7$ (from Section 3.4) showing the tension force acting in the z-direction, $F_{z,tens} = (B_x\partial_x + B_z\partial_z)B_z$, evaluated at $x = 3.0$ and $t = 0.0$ for both positive ($q = 0.5$) and negative ($q = -0.5$) twisted tube. The dashed line shows the pro-file from the symmetrical tube from Section 3.2 where no pumped background field is present.

per side, leading to a net tension force that acts up-wards in concert with buoyancy, encouraging rise. For negatively-twisted flux tubes, the resultant net tension force is downwards, acting against buoyant rise. As ex-plained in Papes 1 and 2, this selection mechanism, when related to the solar context, is in agreement with the so-lar hemispherical helicity rule(s).

With the role of time-averaged pumped background field in creating an asymmetry between the rise of dif-ferently twisted flux tubes firmly established in a canon-ical case above, it is essential to note that the pumped magnetic layer can have significant local temporal and spatial variations, due to turbulent nature of the over-shooting convection. These variations can potentially affect the initial background state that the flux tube experiences quite substantially. One could argue that the results that we presented earlier were not necessar-ily representative since they may be a result of a fa-vorable (or unfavorable) fluctuation in the initial condi-tions. Furthermore, as explained and explored in Paper 2, we might expect substantial variations in behavior, including violations to any "rules" governing the dy-namics. This is not a bad thing, since the Solar Hemi-spherical Helicity Rule that we are trying to understand is itself actually only a statistical rule that is relatively

weakly obeyed, in the sense that there are substantial violations to the rule.

With this in mind, and to better understand the implications of initial conditions, in the full paper we carry out a Monte Carlo-type (MC) study that examines two sources of local variations that can affect the initial background conditions and hence the rise dynamics of the flux tube.

REFERENCES

Abbett, W. P., Fisher, G. H., Fan, Y., & Bercik, D. J. 2004, ApJ, 612, 557

Abramenko, V. I., Wang, T., & Yurchishin, V. B. 1997, SoPh, 174, 291, doi: 10.1023/A:1004957515498

Acheson, D. J. 1979, SoPh, 62, 23, doi: 10.1007/BF00150129

Amari, T., Luciani, J. F., Aly, J. J., Mikic, Z., & Linker, J. 2003, ApJ, 595, 1231, doi: 10.1086/377444

Bao, S., & Zhang, H. 1998, ApJL, 496, L43, doi: 10.1086/311232

Brummell, N. H., Clune, T. L., & Toomre, J. 2002, ApJ, 570, 825

Caligari, P., Moreno-Insertis, F., & Schussler, M. 1995, ApJ, 441, 886, doi: 10.1086/175410

Cattaneo, F., & Hughes, D. W. 1988, Journal of Fluid Mechanics, 196, 323. http://cdsads.u-strasbg.fr/cgi-bin/nph-bib_query? bibcode=1988JFM...196..323C&db_key=AST

Choudhuri, A. R. 1989, 123, 217. http://cdsads.u-strasbg.fr/cgi-bin/nph-bib_query? bibcode=1989SoPh..123..217C&db_key=AST

Choudhuri, A. R., Chatterjee, P., & Nandy, D. 2004, ApJL, 615, L57, doi: 10.1086/426054

Cline, K. S. 2003, PhD thesis, UNIVERSITY OF COLORADO AT BOULDER

Dorch, S. B. F., Gudiksen, B. V., Abbett, W. P., & Nordlund, Å. 2001, A&A, 380, 734. http://adsabs.harvard.edu/cgi-bin/nph-bib_query? bibcode=2001A%26A...380..734D&db_key=AST

D'Silva, S., & Choudhuri, A. R. 1993, A&A, 272, 621. http://adsabs.harvard.edu/cgi-bin/nph-bib_query? bibcode=1993A%26A...272..621D&db_key=AST

Fan, Y., Fisher, G. H., & Deluca, E. E. 1993, ApJ, 405, 390, doi: 10.1086/172370

Fan, Y., Fisher, G. H., & McClymont, A. N. 1994, ApJ, 436, 907, doi: 10.1086/174967

Hale, G. E. 1908, ApJ, 28, 315, doi: 10.1086/141602

Hale, G. E., Ellerman, F., Nicholson, S. B., & Joy, A. H. 1919, ApJ, 49, 153, doi: 10.1086/142452

Hurlburt, N. E., Proctor, M. R. E., Weiss, N. O., & Brownjohn, D. P. 1989, Journal of Fluid Mechanics, 207, 587. http://adsabs.harvard.edu/cgi-bin/nph-bib_query? bibcode=1989JFM...207..587H&db_key=PHY

Hurlburt, N. E., Toomre, J., Massaguer, J. M., & Zahn, J. 1994, ApJ, 421, 245

Korre, L., Brummell, N., Garaud, P., & Guervilly, C. 2021, MNRAS, 503, 362, doi: 10.1093/mnras/stab477

Korre, L., Garaud, P., & Brummell, N. H. 2019, MNRAS, 484, 1220, doi: 10.1093/mnras/stz047

Longcope, D. W., Fisher, G. H., & Arendt, S. 1996, ApJ, 464, 999

Longcope, D. W., & Klapper, I. 1997, ApJ, 488, 443, doi: 10.1086/304680

Low, B. C. 1996, SoPh, 167, 217, doi: 10.1007/BF00146338

Manek, B., & Brummell, N. 2021, ApJ, 909, 72, doi: 10.3847/1538-4357/abd859

Manek, B., Brummell, N., & Lee, D. 2018, ApJL, 859, L27, doi: 10.3847/2041-8213/aac723

Matthews, P. C., Hughes, D. W., & Proctor, M. R. E. 1995, ApJ, 448, 938, doi: 10.1086/176022

Moffatt, H. K. 1969, Journal of Fluid Mechanics, 35, 117–129, doi: 10.1017/S0022112069000991

Moreno-Insertis, F. 1983, A&A, 122, 241

—. 1986, A&A, 166, 291

Moreno-Insertis, F., & Emonet, T. 1996, ApJ, 472, L53. http://adsabs.harvard.edu/cgi-bin/nph-bib_query?bibcode=1996ApJ...472L..53M&db_key=AST

Nindos, A., & Andrews, M. D. 2004, ApJL, 616, L175, doi: 10.1086/426861

Parker, E. N. 1975, ApJ, 198, 205. http://adsabs.harvard.edu/cgi-bin/nph-bib_query?bibcode=1975ApJ...198..205P&db_key=AST

Pevtsov, A. A., Berger, M. A., Nindos, A., Norton, A. A., & van Driel-Gesztelyi, L. 2014, SSRv, 186, 285, doi: 10.1007/s11214-014-0082-2

Pevtsov, A. A., Canfield, R. C., & Metcalf, T. R. 1995, ApJL, 440, L109, doi: 10.1086/187773

Rädler, K. H. 1968, Zeitschrift Naturforschung Teil A, 23, 1841, doi: 10.1515/zna-1968-1123

Seehafer, N. 1990, SoPh, 125, 219, doi: 10.1007/BF00158402

Singh, H. P., Roxburgh, I. W., & Chan, K. L. 1995, A&A, 295, 703

Spruit, H. C. 1981, A&A, 102, 129. http://adsabs.harvard.edu/cgi-bin/nph-bib_query?bibcode=1981A%26A...102..129S&db_key=AST

Tobias, S. M., Brummell, N. H., Clune, T. L., & Toomre, J. 1998, ApJ, 502, L177. http://adsabs.harvard.edu/cgi-bin/nph-bib_query?bibcode=1998ApJ...502L.177T&db_key=AST

—. 2001a, ApJ, 549, 1183. http://adsabs.harvard.edu/cgi-bin/nph-bib_query?bibcode=2001ApJ...549.1183T&db_key=AST

—. 2001b, ApJ, 549, 1183, doi: 10.1086/319448

Vasil, G. M., & Brummell, N. H. 2008, ApJ, 686, 709, doi: 10.1086/591144

Zahn, J.-P. 1991, A&A, 252, 179